A Journal of the Gesellschaft Deutscher Chemiker

Angewandte International Edition GDCh Chemie

www.angewandte.org

Accepted Article

Title: Enhancing the Stability of Aqueous Membrane-Free Flow Batteries: Insights into Interphase Processes

Authors: Rebeca Marcilla, paula navalpotro, carla santana santos, antonio Martínez-Bejarano, murilo alcantara, vanesa muñoz-Perales, santiago Ibañez, Nomnotho Jiyane, Catarina Neves, ruben rubio-presa, thomas quast, Joao Coutinho, and wolfgang Schuhmann

To be cited as: *Angew. Chem. Int. Ed.* **2025**, e202424650

Link to VoR: https://doi.org/10.1002/anie.202424650

WILEY VCH

10.1002/anie.202424650

RESEARCH ARTICLE

Enhancing the Stability of Aqueous Membrane-Free Flow Batteries: Insights into Interphase Processes

Paula Navalpotro*[a], Carla Santana Santos[b], Murilo L. Alcantara[c], Vanesa Muñoz-Perales[a], Santiago E. Ibañez[a], Antonio Martínez-Bejarano[a], Nomnotho Jiyane[b], Catarina M. S. S. Neves[c], Rubén Rubio-Presa[d], Thomas Quast[b], Wolfgang Schuhmann[b], João A. P. Coutinho[c], Rebeca Marcilla*[a]

[a] Dr. P. Navalpotro, Dr. V. Muñoz-Perales, Dr. S. E. Ibañez, A. Martínez-Bejarano, Dr. R. Marcilla,
Electrochemical Processes Unit; IMDEA Energy Institute; Avda. Ramón de La Sagra 3, 28935, Móstoles, Spain
E-mail: rebeca.marcilla@imdea.org; paula.navalpotro@imdea.org

[b] Dr. C. Santana Santos, N. Jiyane, Dr. T. Quast, Prof. W. Schuhmann
Analytical Chemistry - Center for Electrochemical Sciences (CES); Faculty of Chemistry and Biochemistry, Ruhr University Bochum
Universitätsstr. 150, D-44780 Bochum, Germany

[c] Dr. M. L. Alcantara, Dr. C. M. S. S. Neves, Prof. J. A. P. Coutinho
CICECO - Aveiro Institute of Materials, Chemistry Department; University of Aveiro; 3810-193 Aveiro, Portugal

[d] Dr. R. Rubio-Presa
Department of Chemistry; University of Burgos; Pza. Misael Bañuelos s/n, Burgos, E-09001 Spain

Supporting information for this article is given via a link at the end of the document.

Abstract: Membrane-free flow batteries using immiscible electrolytes aim to overcome limitations of conventional redox flow batteries by eliminating expensive ion-selective membranes. However, they face challenges including low power density due to the transport constraints in immiscible electrolytes, the need for high partitioned stable compatible active species, and the overlooked self-discharge interphase phenomena that reduces coulombic efficiency. We present a novel aqueous biphasic system based on two salts improving electrolyte ionic conductivity and viscosity. Potassium ferrocyanide ($K_4[Fe(CN)_6]$) and a sulfonated viologen ($(SPr_2)V$) species were examined computationally and experimentally demonstrating effective redox pairs separation in all oxidation states, achieving a tenfold higher concentration in their electrolyte. The mutual compatibility and stability of these species enabled unprecedented scanning electrochemical microscopy (SECM) analysis of the liquid-liquid interphase revealing insights like species concentration gradients and crossover. The enhanced electrolyte properties expanded the open-circuit voltage to 1.1 V and improved mass transport, enabling power densities that are 3.5 times higher than previous examples. The battery achieved 80.2% energy efficiency at C/2 rate and under flowing conditions it maintained stable performance over a month (400 cycles) at high states of charge. This work presents an innovative aqueous membrane-free flow battery that avoids parasitic reactions, enabling detailed interphase studies and advancing this technology.

Introduction

The pressing energy transition towards the decarbonization of the global energy infrastructure has driven the growing penetration of sustainable yet intermittent energy sources into the electricity grid.[1] Large-scale and stationary electrochemical energy storage play a crucial role to sustain the efficient, low-cost and reliable delivery of renewable energy.[2] Redox flow batteries (RFB) are a promising electrochemical technology for scalable energy storage (>6 h). Their ability to decouple power and energy density positions them ahead of enclosed batteries for grid-scale energy storage providing high efficiency, flexibility and modularity.[3,4] Among the different RFB technologies, all-vanadium RFB (VRFB) are the most widely deployed.[5] VRFB are composed of acidic vanadium-based electrolytes separated by a Nafion ion-exchange membrane for preventing cross-mixing of electrolytes while facilitating the ion transport to maintain charge balance[6]. Despite their technological maturity and appealing features, the massive deployment of VRFB is still hampered by their high costs, mainly associated with the high and fluctuating price of vanadium-based electrolyte, and the high cost of ion-exchange membranes, comprising ~40% of the battery price.[7] Other limitations are the declaration of vanadium as a critical raw material,[8] the corrosive character of acidic electrolytes[9] and their narrow operation temperature typically of 10°C up to 40°C.[10,11]

Among the possible alternative chemistries, aqueous organic redox flow batteries (AORFB) have emerged as a promising solution by replacing vanadium species with organic redox molecules composed of abundant elements, offering potential advantages in sustainability and cost.[12–14] Molecular engineering allows to tailor the molecular structure of these active materials to tune key properties such as solubility, stability, and redox potential in alkaline, acidic or neutral AORFB. However, AORFB also face several challenges, particularly regarding their long-term performance. The stability of AORFB is often limited by rapid capacity fading due to active species degradation, and cross-contamination through the membrane.[15–18] While active species are typically selected based on their electrochemical and chemical stability in the supporting electrolytes, the chemical compatibility between the active species of the catholyte and anolyte remains largely

10.1002/anie.202424650

overlooked. Moreover, achieving complete separation of organic molecules with conventional ion-selective membranes is very challenging because their cross-migration is thermodynamically favored, especially for small molecules. In the context of neutral-pH AORFB, commonly used chemistries are limited to viologen derivatives as anolyte species, paired with TEMPO derivatives, ferrocene derivatives, or ferrocyanides as catholyte species.[19–23] Notably, only the redox couple comprising ferrocyanide and a sulfonated viologen derivative ($(SPr_2)V$) has demonstrated mutual compatibility in neutral pH electrolytes, enabling their use as mixed electrolytes in highly stable symmetric AORFB.[24]

Another strategy to decrease the high cost of VRFB is the development of membrane-free RFBs which do not employ any kind of membrane or physical separator.[25] Unlike conventional RFBs where the ion-selective membrane counteracts thermodynamics to prevent crossover, in the membrane-free approach the separation of the active species is achieved solely by thermodynamics using immiscible biphasic electrolytes and organic redox species with high partitioning coefficients. The first attempts involved aqueous-nonaqueous immiscible systems containing various active species such as quinones, viologens, TEMPO derivatives, and metal salts.[26–32] This concept was further extended to aqueous-aqueous immiscible redox electrolytes, providing a more sustainable, environmentally friendly, and cost-effective battery chemistry.[33,34] Recently, we reported the first entirely aqueous membrane-free flow battery utilizing an aqueous biphasic system (ABS) based on polyethylene glycol (PEG) and using methyl viologen and a ferrocene derivative as anolyte and catholyte redox species, respectively.[35] However, the PEG-rich phase of the ABS exhibited low conductivity and high viscosity, which limited the maximum applied current and the output power of the battery. Additionally, while the active species showed adequate partition coefficients, their low chemical compatibility led to self-discharge and degradation due to parasitic reactions at the interphase, resulting in a low coulombic efficiency (CE ≤ 68%) and moderate long-term performance of the battery.

This work introduces a new aqueous biphasic system (ABS) composed of two salts, that enables the use of compatible and stable active species, namely potassium ferrocyanide ($K_4[Fe(CN)_6]$) and 1,1-bis(3-sulfonatopropyl)-4,4′-bipyridinium ($(SPr_2)V$) (Figure 1). The compatibility of the selected redox pairs avoids parasitic reactions and facilitates a controlled and simplified interpretation of the complex phenomena occurring at the liquid-liquid interphase. The partitioning behavior of the active species in all oxidation states, determined by the first time through both computational and experimental methods, confirmed their suitable partition coefficients. Moreover, substituting PEG with a salt resulted in immiscible electrolytes with increased ionic conductivities and lower viscosities, thereby improving overall transport properties. The characterization of this aqueous membrane-free battery under static and flow conditions confirmed their improved performance exhibiting enhanced power and robust long-term stability throughout 400 cycles (33 days). More importantly, the use of these immiscible redox electrolytes provides unprecedented insights into processes at the liquid/liquid interphase, such as concentration gradient of the active species and self-discharge phenomena, using scanning electrochemical microscopy (SECM) for the first time.

Results and Discussion

Aqueous biphasic system

Formation of the aqueous biphasic system (ABS)

A new ABS was prepared by mixing lithium bis(trifluoromethanesulfonyl)imide (LiTFSI) and $(NH_4)_2SO_4$ in water. The system separated into two aqueous phases due to a salting-out effect, a well-known phenomenon that occurs when two salts with different interactions with water are dissolved in the same solution.[36] Figure 2a illustrates the experimentally obtained binodal curve, where any mixture point above this curve undergoes phase separation into two immiscible aqueous phases. A mixture point comprising 30 %wt LiTFSI, 20 %wt $(NH_4)_2SO_4$, and 50 %wt H_2O was selected, and the composition of each newly formed phase was analyzed using ion chromatography. Figure 2b shows that the top phase (TP) consists of Li^+, NH_4^+ and SO_4^{2-} with a negligible amount of $TFSI^-$, whereas the bottom phase (BP) consists mostly of NH_4^+ and $TFSI^-$, with lower amounts of Li^+ and SO_4^{2-}.

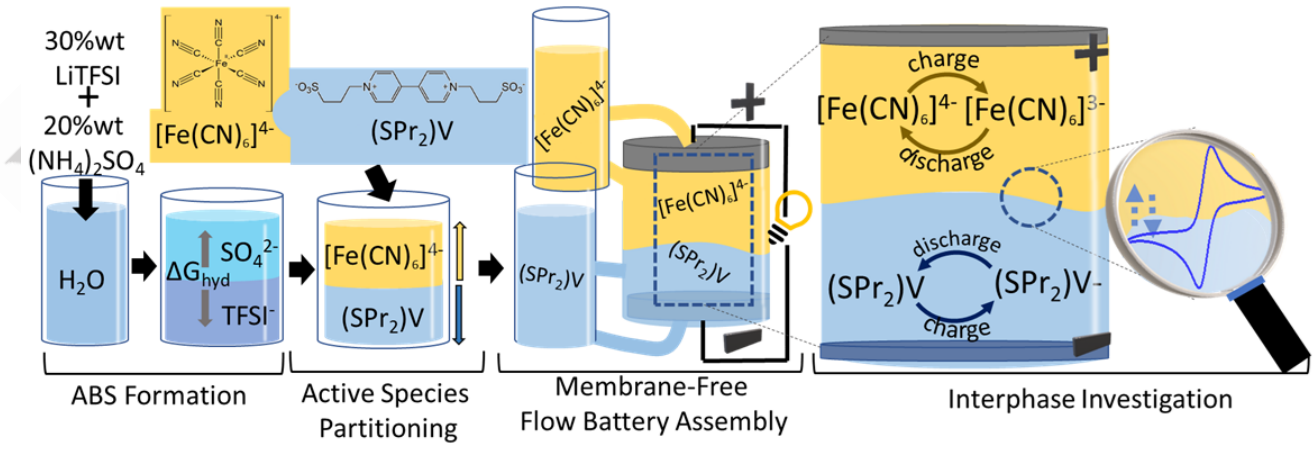

Figure 1. Representation of the preparation of the aqueous membrane-free flow battery and the aspects addressed in this work.

10.1002/anie.202424650

Unlike common ABS, where each phase is typically enriched with a specific solute, this system exhibits a pronounced ion exchange between the two immiscible phases. This is evidenced by the significant change in the slope of phase-binodal curve with increasing $(NH_4)_2SO_4$ concentration. The ion exchange is characterized by the partition of Li^+ from the BP to the TP, counterbalanced by the migration of NH_4^+ from the TP to the more hydrophobic BP. This behavior was expected, given that among the ions present in the solution NH_4^+ and $TFSI^-$ exhibit less negative Gibbs hydration energies (trend: $SO_4^{2-} > Li^+ > NH_4^+ >> TFSI^-$ [37]). Consequently, NH_4^+ and $TFSI^-$ are more likely to preferentially partition into the more hydrophobic BP. The partition of solutes in biphasic systems, in the absence of specific interactions, is dominated by solute polarities and phase hydrophobicities. While this is commonly observed in organic-aqueous systems, the principle remains valid here, as the $TFSI^-$rich phase is significantly more hydrophobic than the salt-rich phase. The ions with more concentrated charges (i.e., more negative Gibbs hydration energies) partition preferentially towards the more hydrophilic salt-rich phase (e.g., Li^+ and SO_4^{2-}), while ions with dispersed charges (i.e., less negative Gibbs hydration energies) partition preferentially towards the more hydrophobic TFSI-rich phase. The two phases of the newly developed ABS show high ionic conductivity σ and low viscosity η (see Table S1, Figure S2). Specifically, the TP has a high σ (158 mS cm^{-1}) and low η (3.18 mPa·s), compared to the low conductivities < 10 mS cm^{-1} and high viscosities ~20 mPa·s of reported ABS.[38]

Partition behaviour of active species

The partition coefficient (*K*) of the selected active species in their different oxidation states, $Fe^{II}(CN)_6^{4-}$//$Fe^{III}(CN)_6^{3-}$ and $(SPr_2)V$//$(SPr_2)V^-$, were determined by UV-Vis spectroscopy (Figure S3). The results evidenced the higher affinity of the catholyte species, $[Fe(CN)_6]^{3-}$//$[Fe(CN)_6]^{4-}$ for the TP (*K>10*), and the higher affinity of the anolyte species $(SPr_2)V$//$(SPr_2)V^-$ for the BP (*K<0.01*) (Figure 2c), ensuring their efficient thermodynamically-driven separation. The affinity of the $(SPr_2)V$ species for the BP is particularly high, leading to cross-migration concentrations in the TP that were difficult to detect with UV-Vis spectroscopy. Figure 2d illustrates the charge density distributions of the studied redox active species, evidencing the polarity differences between the two active species. The reddish areas represent highly negatively charged sites of the molecule (hydrogen bond acceptors), the bluish areas indicate positively charged sites, and the green areas correspond to predominant non-charged regions of the surface. $Fe^{II}(CN)_6^{4-}$ displays a predominantly reddish color due to its high negative charge (-4), whereas $Fe^{III}(CN)_6^{3-}$, with a slightly less negative charge (-3), exhibits an overall reddish appearance but includes a yellowish central core, reflecting its lower charge density. For $(SPr_2)V$, two red sites correspond to the $-SO_3$ radicals, while a bluish region is observed around the viologen core, indicating that the positive charge of this zwitterion is more dispersed around its core. In contrast, $(SPr_2)V^-$ shows a greener central core, reflecting a more negative charge distribution.

Sigma profiles (Figure 2d) further quantify these differences by illustrating the probability distribution of surface charge densities. Compared to $[Fe(CN)_6]^{3-}$, $[Fe(CN)_6]^{4-}$ presents a larger area of highly induced charge densities, reinforcing its stronger electrostatic interactions. Similarly, $(SPr_2)V$ exhibits a higher concentration of positive charges (negative induced charge density) compared to $(SPr_2)V^-$. Notably, both the reduced viologen $(SPr_2)V^-$ and the oxidized $[Fe(CN)_6]^{3-}$ show smaller areas of highly concentrated charges compared to their original forms, suggesting a reduction in strong electrostatic interactions upon redox transitions. This effect decreases the partitioning tendency of both species toward their respective phases (Figure 2c), indicating that the battery in its discharged state (containing $Fe^{II}(CN)_6^{4-}$ and $(SPr_2)V$) is likely to experience lower cross-contamination compared to when it is fully charged. In addition, computational predictions using the COSMO-RS (conductor-like screening model for real solvents) model[39,40] were conducted to assess the partitioning behavior of ferrocyanide and viologen derivatives in this specific ABS (Figure 2c,d). Santiago et al.[41] observed that the major source of error in partition coefficient predictions by COSMO-RS is related to the correct quantification of species concentrations in both phases of the biphasic system. Our previous study[42] showed that COSMO-RS correctly predicts the phase to which the redox-active species in ABS partition, including viologen, anthraquinone, and TEMPO. However, from a quantitative perspective, the model exhibits deviations typically up to two orders of magnitude, with most viologen derivatives showing deviations within one order of magnitude.

In the COSMO-RS simulations applied herein, the compositions of species in the two phases at equilibrium were the actual concentrations measured by ion chromatography (Figure 2b, detailed errors bars in Figure S4)). Using experimental concentrations not only reduced prediction deviations but also allowed for a more precise quantification of ion exchange between Li^+ and NH_4^+. Figure 2c shows that COSMO-RS correctly predicted the phases to which all active species selectively partition. Moreover, it estimated the order of magnitude of this partitioning for three of the four species. The exception was the zwitterion $(SPr_2)V$ (net charge = 0), for which the model adequately predicted the preferred phase but drastically overestimated the partition coefficient. The zwitterionic nature of $(SPr_2)V$ introduces local charges and intermolecular interactions, challenging the quantitative accuracy of most predictive models. Nevertheless, the qualitative accuracy of COSMO-RS underscores its ability in assessing complex aqueous biphasic systems. The model was also able to predict the partitioning of both ferrocyanide and viologen redox pairs in their different oxidation states, into the TP and BP, respectively (Figure 2c). The sigma profiles also reveal the influence of induced charge effects, where highly negative anions, such as $[Fe(CN)_6]^{4-}$, exhibit large areas of highly positive charge densities (p(σ)), further emphasizing the role of electrostatic interactions in solvation and partitioning shown in Figure 2c.

These results demonstrate the effective selective partitioning of the active species, in both their "*uncharged*" and "*charged*" states, within their respective electrolytes. This minimizes cross-contamination not only during the assembly of the battery but also during its operation, when the active species undergo oxidation

10.1002/anie.202424650

and reduction. It is important to note that initial attempts to use previously reported ABS[34,35] for assembling membrane-free batteries with $K_4[Fe(CN)_6]$ and $(SPr_2)V$ were unsuccessful, as both active species exhibited a strong affinity for the same BP, preventing effective separation (Figure S5). Both the charge density distribution maps and the sigma profiles generated in this work are available in the supplementary materials.

Electrochemical properties of redox ABS

The mutual compatibility of active species, $K_4[Fe(CN)_6]$ and $(SPr_2)V$, was initially investigated using cyclic voltammetry (CV) in 1 M KCl as electrolyte containing both compounds (Figure S6). Two reversible redox peaks at -0.6 and 0.3 V *vs.* Ag/AgCl (3M KCl), corresponding to the redox reactions of the viologen and ferrocyanide derivatives, respectively, remained stable for multiple cycles, confirming the compatibility of these compounds. In contrast to most of the organic active species, some viologen derivatives and the ferrocyanide compounds do not suffer from parasitic reactions when they are mixed in the same electrolyte showing no degradation.[24,43] The electrochemical properties of the newly developed ABS were then assessed by performing CV in each of the two immiscible electrolytes. The BP (anolyte) exhibits a reversible redox process at -0.77 V *vs.* Ag/AgCl (3M KCl), attributed to the viologen $(SPr_2)V$, which remains stable upon cycling (Figure S7a). The TP (catholyte) also exhibits a reversible peak at 0.35 *vs.* Ag/AgCl (3 M KCl) corresponding to

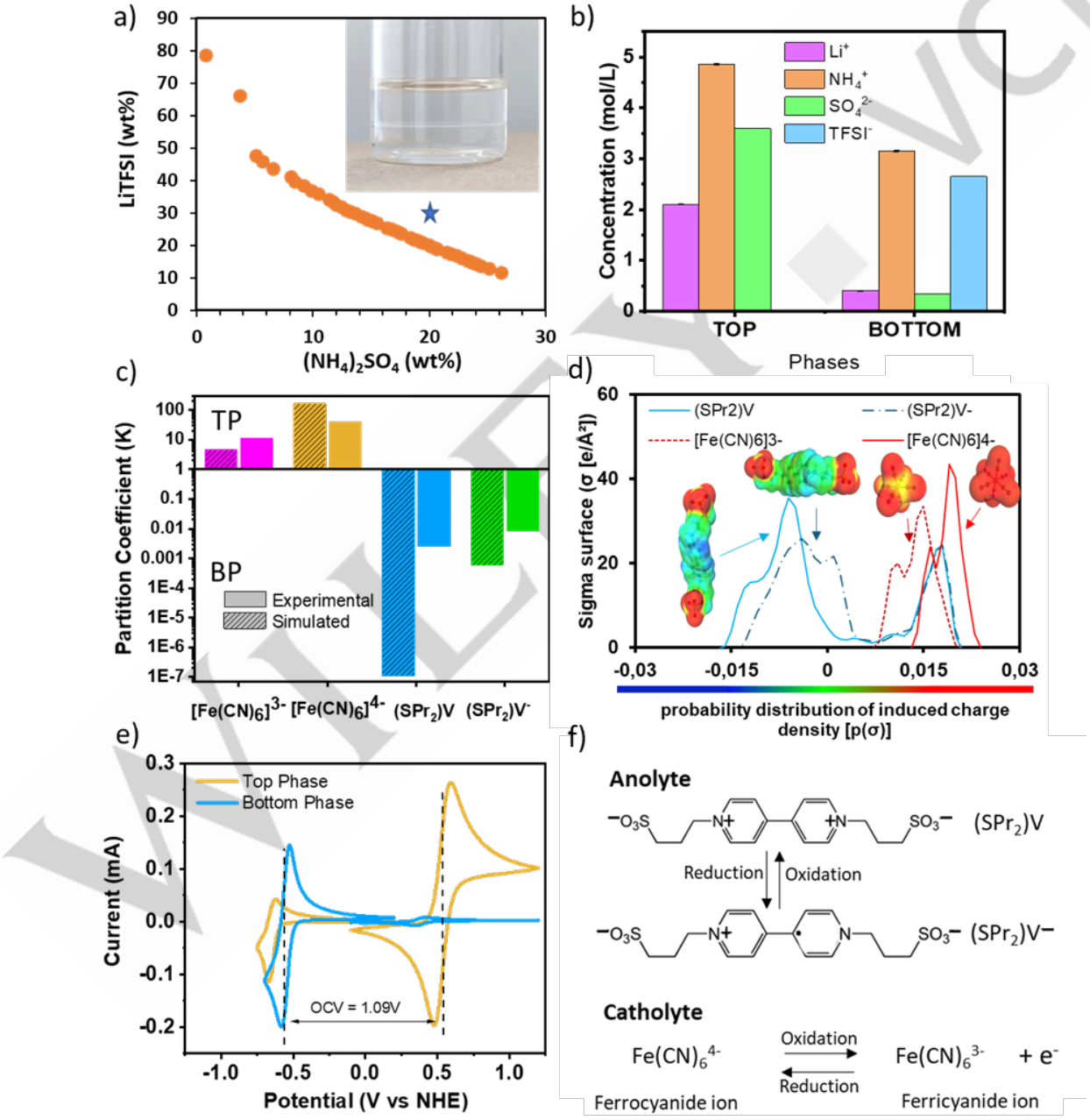

Figure 2. a) Binodal curve. Inset: Digital photo of the biphasic system at a selected mixture point: 30%wt LiTFSI + 20% wt $(NH_4)_2SO_4$ + 50%wt H_2O. b) Phase composition analyzed by ion chromatography including error bars (more detailed view in Figure S4). c) Partition coefficient of active species obtained by UV-Vis

spectroscopy and simulated values predicted by COSMO-RS. d) Charge density distribution and sigma profile of the active species obtained with COSMO-RS. e) CV of anolyte and catholyte (pH 7) at 0.1 M active species concentration and 10 mV s^{-1}. f) Scheme of the redox reactions of the active species.

the redox reaction of $K_4[Fe(CN)_6]$. However, the shape of the CV changes significantly with the number of cycles, with a noticeable decrease in peak current and a slight increase in the separation between the anodic and cathodic peaks (Figure S7b). This behavior is likely due to the reported instability of ferro-ferricyanide in the slightly acidic electrolyte (pH ~4.7- 4.8) (Table S1).[44] When the pH of the ABS was adjusted to 7, which is reported as the most favorable pH,[45–48] the stability of the catholyte significantly improved, with CVs remaining invariant over 1000 cycles (Figure S7c). The CVs of the two immiscible electrolytes reveal one reversible peak at 0.54 V (*vs* NHE) associated with the $[Fe(CN)_6]^{4-}$ in the catholyte top phase (TP), and another peak at -0.55 V (vs NHE) attributed to $(SPr_2)V$ in the anolyte BP (Figure 2e,f). This suggests a theoretical open-circuit voltage (OCV) as high as 1.09 V. Notably, this value is 220 mV larger than the OCV of a conventional flow battery with similar active species,[24,43,49] which is due to the shift of the redox potential in the highly concentrated electrolytes (see Figure S8). Interestingly, a small signal from the active viologen species appears in the CV of the catholyte (TP) and vice versa, which is consistent with the high partition coefficient of the active species.

Further investigation with respect to the diffusion coefficient (*D*) and kinetic (k^0) parameters of the electrolytes supports the anticipated benefits of the new ABS composition (Figure S9). The low viscosity of the biphasic electrolytes, particularly in the TP, leads to a diffusion coefficient for the active species in the catholyte (TP) that is an order of magnitude higher than the previously reported values for other membrane-free RFB (Table S1). The calculated values using glassy carbon electrodes of the diffusion coefficient ($D_{[Fe(CN)6]4-} = 1.11 \cdot 10^{-6}$ cm^2/s and $D_{SPr2V} = 1.10$ 10^{-6} cm^2 s^{-1}) and kinetic constants ($k^0_{[Fe(CN)6]4-} = 9.11 \cdot 10^{-4}$ cm/s and k^0_{SPr2V} = 0.036 cm s^{-1}) are within the same range as those reported for conventional RFB.[24,49]

Unravelling the active species transport through the liquid-liquid interphase

Scanning Electrochemical Microscopy (SECM) has been demonstrated to be a powerful tool for monitoring electron transfer at the interface between two immiscible liquids.[50–55] Here, a SECM set-up placed inside a glovebox (oxygen free) is employed to investigate the dynamics of the redox species in each phase and at the interphase of a membrane-free RFB.

This investigation was possible due to the newly formulated immiscible electrolytes with compatible species that enable the study of interphase processes without interference from parasitic or irreversible reactions and allowed to interpret the interphase phenomena in a controlled and simplified experimental framework. Figure 3a and Figure S10 illustrate the experimental set-up, where a polarized needle-type SECM tip is used to monitor the electrochemical processes of the active species present in the electrolyte. To investigate crossover, only one of the redox species is dissolved in the ABS before testing. The SECM tip was placed in the bulk of either the TP or BP, and a CV was conducted to observe the characteristic redox process of the added compound (Figure S11). The increased current measured at the SECM tip correlates with the presence of the redox species, shedding light on the crossover between phases. Under these conditions, the CVs show only a single process associated with the specifically added redox compound. Figure S12 shows that the current associated to the redox processes of the viologen derivative $(SPr_2)V^-$ // $(SPr_2)V$ was higher in the BP than in the TP, whereas the current associated with the $[Fe(CN)_6]^{4-}$ // $[Fe(CN)_6]^{3-}$ redox pair was higher in the TP. These results are in agreement with the partition results discussed above (see Figure 2c and 2e). To investigate the interphase region, the SECM tip was polarized at a constant potential while being moved from the TP to the BP in 1 µm increments (Figure 3a). Depending on whether $(SPr_2)V$ or $[Fe(CN)_6]^{4-}$ was added to the ABS, the SECM tip was polarized at -700 mV or +700 mV, respectively. The steady-state current was used to monitor the presence of the active species in the bulk of the immiscible electrolytes and in the interphase. As shown in Figure S12a, the normalized current dropped sharply from 1 to nearly 0 as the tip moved from one phase to the other, clearly indicating the high partition coefficient of $(SPr_2)V$ to the bottom phase and of $[Fe(CN)_6]^{4-}$ to the top phase. A similar sharp change in the SECM tip current response was observed when both redox species were present at 0.1 M in the biphasic system (Figure 3b). This sharp transition confirms the consistent partitioning of the species in the biphasic system. By traversing the interphase from the TP to the BP, we estimated the thickness of the interphase reflecting the concentration gradient for both $(SPr_2)V$ and ferrocyanide to be approximately 1 µm. This value likely reflects the resolution of the SECM positioning system and may also be influenced by disturbances at the SECM tip caused by the surface tension. Grimaud and co-workers employed Raman spectroscopy to map the electrolyte ions in the interface between two immiscible electrolyte solutions, showing an inverse correlation of the interface thickness with the salts concentration, with values in the range of 2-10 µm,[56] which is in close agreement with the SECM results. The observed thinner interphase is indicative of a system exhibiting stronger ion partitioning.[56]

During battery charging, the active species $[Fe(CN)_6]^{4-}$ and $(SPr_2)V$ are converted to $[Fe(CN)_6]^{3-}$ and $(SPr_2)V^-$, respectively. These species might also cross through the interphase, leading to rapid capacity fade. To evaluate the partitioning of the charged species in the ABS, SECM experiments were performed by adding either $[Fe(CN)_6]^{3-}$ or $(SPr_2)V^-$ to the ABS and applying a constant potential to the SECM tip. Figure S12b shows the current associated with the anodic process in the BP (oxidation of $(SPr_2)V^-$ measured at E_{tip} = 0 mV, blue squares) and a sharp decrease in current as the SECM tip crosses the interphase. This result confirms the high partition coefficient of $(SPr_2)V^-$, indicating its high affinity for the BP. In contrast, the reduction process of $[Fe(CN)_6]^{3-}$, manifested by high reduction currents (at E_{tip} = 0 mV, red triangles), was observed in both phases which is consistent with the experimentally measured and simulated partition coefficients, which was lower for $[Fe(CN)_6]^{3-}$ compared to the other species. Although the current values generally correlate with species concentration, the different diffusion coefficients of the species in each phase complicate the quantitative analysis.

10.1002/anie.202424650

RESEARCH ARTICLE

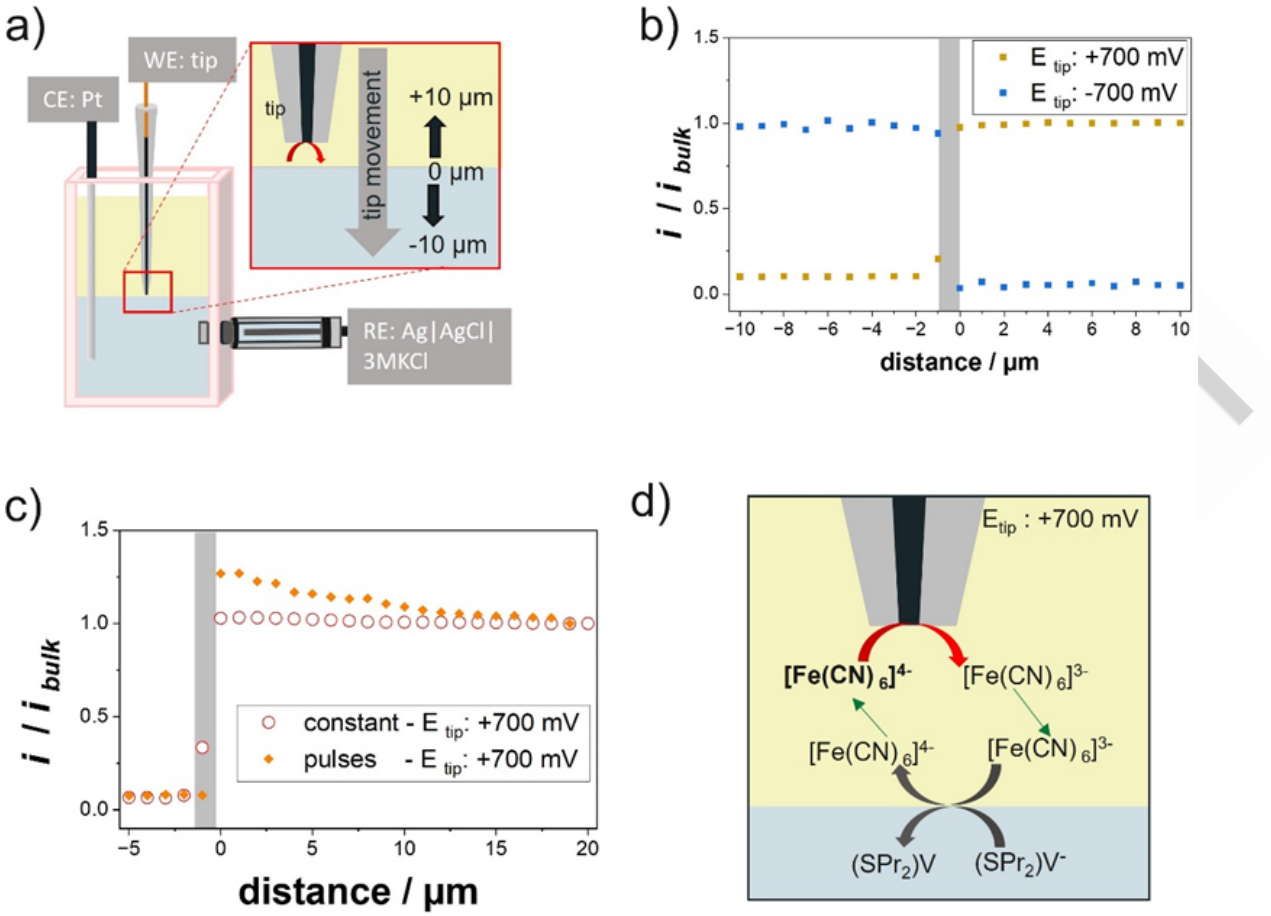

Figure 3. a) Scheme of the SECM cell for studying the interfacial region of the biphasic system, where a needle-type carbon fiber microelectrode was employed as SECM tip (disc diameter of 7 µm and RG <1). b) Normalized SECM tip current vs. distance (SECM curves) recorded in the biphasic system with dissolved 0.1 M $[Fe(CN)_6]^{4-}$ + 0.1 M $(SPr_2)V$. The SECM tip was polarized at +700 mV (yellow data) or –700 mV (blue data) vs. Ag|AgCl|3 M KCl. c) SECM curves performed in the biphasic system containing 0.1 M $[Fe(CN)_6]^{4-}$ + 0.1 M $(SPr_2)V^-$ obtained by polarizing the tip constantly at +700 mV (circle dots) and following a potential pulse program of 10 s applying –700 mV and sequentially +700 mV for 10 s (orange data). d) Schematic of the local regeneration process of $[Fe(CN)_6]^{4-}$ at the interphase due to the reaction with the reduced form of $(SPr_2)V$.

The low coulombic efficiency associated with the self-discharge of "charged" active species at the interphase is a critical challenge in membrane-free battery technology.[34] This phenomenon consists of a spontaneous electron-exchange reaction that occurs when the charged species come into contact at the liquid-liquid interphase, reverting to the discharged state and inducing changes in the concentration of active species in the vicinity of the interphase. To investigate the dynamics of species near the interphase during battery operation, SECM analyses were conducted in ABS containing active species at different state of charge. Given the high complexity of performing experiments at the liquid-liquid interphase, an initial simplified experiment was carried out using a biphasic system with $[Fe(CN)_6]^{4-}$ in the TP (discharged catholyte) and $(SPr_2)V^-$ in the BP (charged anolyte). Both species showed low crossover and high partitioning behavior (Figure 3b and S10b). Figure S13 shows that the oxidation current associated with $(SPr_2)V^-$ (E_{tip} = 0 mV) in the presence of $[Fe(CN)_6]^{4-}$ showed a similarly sharp transition as observed when measured alone (Figure S12b), suggesting chemical compatibility with $[Fe(CN)_6]^{4-}$. The response obtained when the SECM tip was polarized at +700 mV (oxidation of $[Fe(CN)_6]^{4-}$ and $(SPr_2)V^-$ also showed a constant current in the TP and BP, with a drastic decay when the tip crossed the interphase (Figure 3c, red circles). A similar SECM experiment was repeated but using a pulsed potential, where the tip was polarized at -700 mV for 10 s, followed by polarization at +700 mV for 10 s prior to the current acquisition (Figure 3c, orange diamonds). Under these conditions, the tip converted any SPr_2V to SPr_2V^- in tip vicinity polarized at -700 mV, promoting a local $(SPr_2)V^-$ enrichment. Subsequently, oxidation of $[Fe(CN)_6]^{4-}$ and SPr_2V^- occurred when the tip was polarized at +700 mV. Interestingly, the normalized SECM tip current at +700mV increased as the tip moved from the TP to the BP, approaching the interphase suggesting a higher concentration of $[Fe(CN)_6]^{4-}$ in the interfacial region (Figure 3c, orange diamonds). This might be explained by the mechanism proposed in Figure 3d. At +700 mV the tip generates $[Fe(CN)_6]^{3-}$, which meets SPr_2V^- diffusing from the BP and undergoes an electron exchange reaction being reconverted into $[Fe(CN)_6]^{4-}$. Consequently, the SECM tip current for $[Fe(CN)_6]^{4-}$ oxidation increases as the tip approaches the interphase. This regeneration of $[Fe(CN)_6]^{4-}$ was not observed when the tip was constantly polarized at +700 mV (circle data in Figure 3c), as constant polarization depletes SPr_2V^- near the tip, preventing the electron exchange reaction between $[Fe(CN)_6]^{3-}$ and SPr_2V^-. No regeneration of $[Fe(CN)_6]^{4-}$ was detec-

ted during the constant polarization experiment, unlike with the pulse-based method. The SECM results provide an in-situ evidence that the recombination reaction between the charged species $[Fe(CN)_6]^{3-}$ and SPr_2V^- at the interface is responsible for the self-discharge process in membrane-free immiscible batteries.

Performance of the membrane-free battery

Static membrane-free battery

To assess the suitability of this newly developed ABS for application in a membrane-free battery, 0.1 M $[Fe(CN)_6]^{4-}$ and 0.1 M $(SPr_2)V$ were dissolved in the ABS (1.5mL each phase) prior to the assembly of a *static* battery. The *static* battery was charged and discharged at different current densities, showing a flat voltage plateau for both the charge and discharge processes (Figure 4a). At low current densities, the discharge voltage was close to the theoretical value of 1.08 V. Figure 4b shows the rate capability of the static battery with increased discharge capacity and higher coulombic efficiencies (*CE*) as the C-rate increases, reaching a maximum *CE* of 91.7% at 2C (5.4 mA cm^{-2}). This unconventional trend is attributed to self-discharge due to the recombination of active species at the interphase. The enhanced transport properties of these newly developed biphasic electrolytes resulted in lower battery resistance, enabling a 2.5 times higher current density (2 vs 5.4 mA cm^{-2}) compared to previously reported examples,[34,35] while maintaining a stable and efficient performance. Additionally, the improved mass transport properties of this ABS allowed reaching a voltage efficiency as high as 80.2% at C/2 (Figure 4c) with the optimal operation conditions for the battery at C/2 reaching a CE of 75%, a voltage efficiency (VE) of 80% and an energy efficiency (EE) as high as 60%. These values represent a significant improvement of membrane-free batteries.[35] Figure 4d shows the cyclability of the battery at C/2 (1.34 mA cm^{-2}), demonstrating consistent and stable performance with similar charge-discharge profiles, exhibiting clear voltages plateaus and maintaining a constant discharge capacity around 0.6 mAh over 160 cycles. The *CE* remained in average at 75% (Figure 4e). Analysis of the individual potentials of the catholyte, interphase and anolyte during cycling (Figure 4f) shows an increase in the overpotential of the catholyte while the potential of the anolyte remains unchanged. This is likely due to the accumulation of charged species in the catholyte caused by an imbalance in charged species concentration between anolyte and catholyte. This imbalance arises from the well-known high sensitivity of viologens to dissolved oxygen, which oxidizes viologen and reduces the concentration of its reduced form.

Membrane-free redox flow battery

The performance of the battery was investigated under flowing conditions using a flow-thought reactor[57] designed specifically for biphasic membrane-free batteries (Figure S14). Upon galvanostatic cycling at 3 mA cm^{-2}, the battery exhibits rapid capacity fade from the first cycle (Figure S15a). This performance was likely due to parasitic reactions by the reduced viologen species that can be re-oxidized by oxygen. This would cause a misbalance in the SOC of both electrolytes[19] with the SOC of the catholyte continuously increasing during cycling. Although the electrolytes are purged with Ar prior to use, the battery was assembled outside the glovebox. To confirm this hypothesis, two additional experiments were conducted during cycling (Figure S15b). In the first experiment 4 mL of fresh catholyte (equivalent to 20% capacity or 10.72 mAh) was added, and cycling was restarted. This led to an immediate increase in capacity suggesting that the catholyte was the limiting electrolyte during charging, and supporting the hypothesis that oxygen caused electrolyte misbalance. In the second experiment, the battery's upper cut-off voltage was raised during charging provoking battery overcharging followed by cycling (Figure S15b,c).

During this overcharging period, the oxygen evolution reaction is occurring at the cathode while the viologen is being reduced in the anolyte. After the overcharging period, the battery capacity also increased, supporting the idea that overcharging could correct the imbalance caused by the contribution of oxygen to the capacity loss. Both tests suggested that the battery misbalance associated to the presence of oxygen in the negative electrode was the primary cause of the observed capacity decay. This was previously suggested by the increasing on the catholyte overpotential during cycling in the static battery (Figure 4f). To prevent atmospheric oxygen from reacting with the electrolyte, the entire cell was operated inside an argon-filled glovebox. Additionally, both electrolyte solutions were also prepared inside the glove box. Electrochemical impedance spectroscopy (EIS) showed a stable internal resistance of the battery of 1.2 Ω (first point at high frequency, first interception point with X-axes), independent of the flow rate (Figure S16a,b). Discharge polarization experiments revealed a peak power density of 10 mW cm^{-2}, that is not affected by the flow rate (Figure S16c). However, similar to other flow battery systems[58,59], increasing the flow rate from 12 mL min^{-1} to 40 mL min^{-1} could mitigate mass transport limitations, allowing the battery to operate at slightly higher current densities. The results leverage the improved electrolyte properties, leading the battery to achieve a three times higher current density and 3.5 times higher peak power density compared to previously reported aqueous flow membrane-free batteries [35]. The deep charge/discharge voltage profile of the battery from 0% to 100 %SOC at two different current densities under flowing conditions (Figure S16d) allows to observe the color changes in the electrolytes and the stable interphase between them (Figures 5a-b). The anolyte (BP) is clearly identified by the strong blue coloration of reduced viologen, which turns light yellow upon discharge. During the long cycling test at 3 mA cm^{-2} (Figures 5c, S14e), the battery maintained an average *CE* of 70% with no significant capacity fade over more than 400 cycles, equivalent to a one month of testing. This demonstrates its stable performance compared to previously reported (non-hybrid) membrane-free batteries (Table S2). Despite the improved properties of the aqueous electrolytes used such as lower viscosity and improved diffusion, an increase in self-discharge and a lower *CE* were

10.1002/anie.202424650

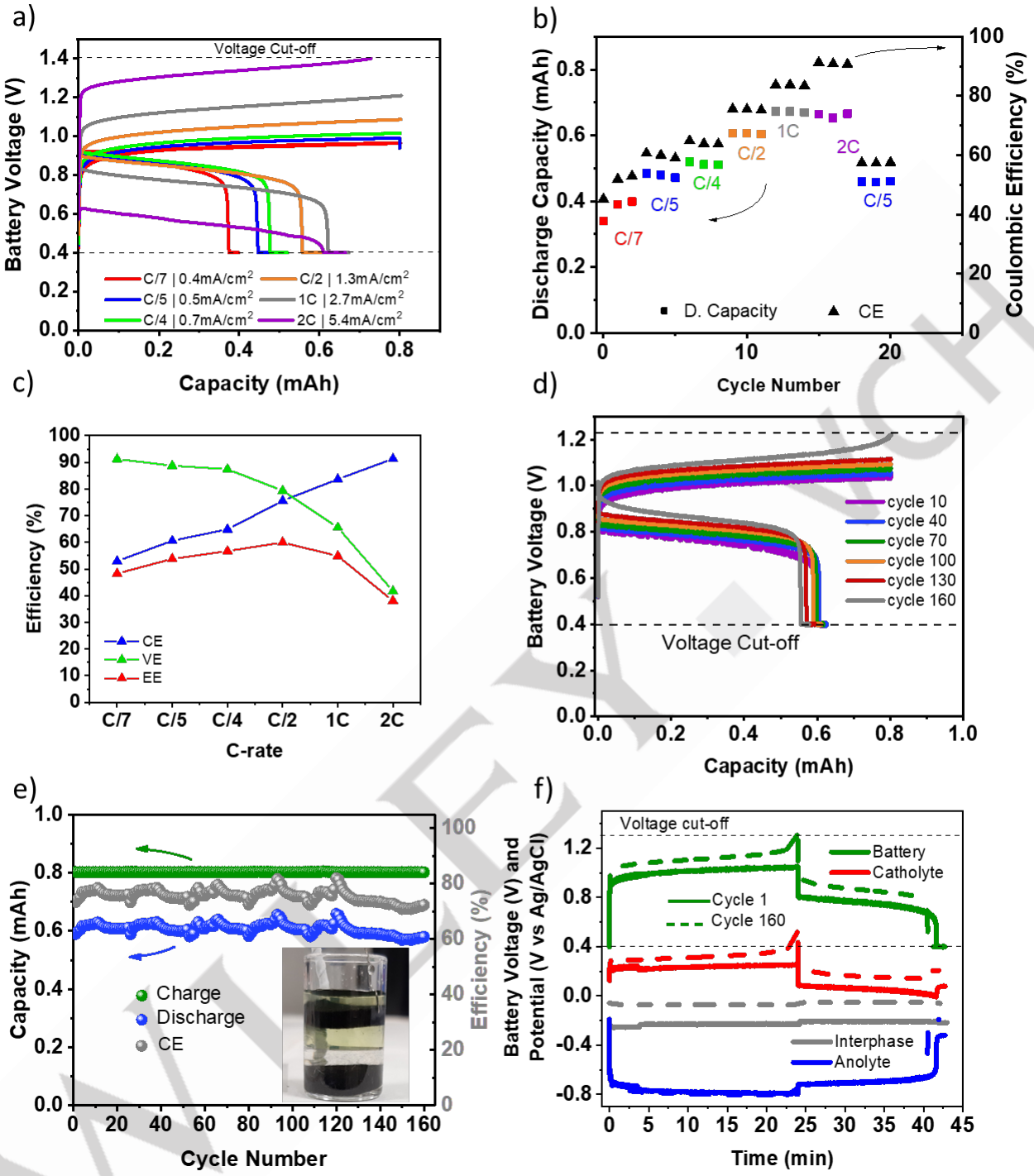

Figure 4. Static battery performance at pH7, 0.1M active species concentration, and 20%SOC. a) Charge-discharge profile at different current densities (C-rate). b) Rate performance. c) Efficiency analysis at different C-rates. d) Cyclability test at C/2 (CCCV). e) Voltage profile of the battery during cyclability test. f) Battery voltage and potential of each electrolyte and the interphase at 1st and 160th cycles.

expected. However, the primary goal of this work was not to maximize the *CE* but to gain deeper insights into the processes at the liquid-liquid interphase.

In contrast to the experiments conducted outside the glove-box (Figure S15), no capacity decay was observed during the long-term cycling, confirming that the presence of oxygen was the source of the observed capacity losses. In the cycling experiment the charge capacity was fixed to 50% SOC while the discharge capacity corresponded to the available capacity until full discharge. The appearance of bubbles attributed to pressure differences induced by the peristaltic pump leads to fluctuations in both discharge capacity and *CE* values (Figure 5c). However, these fluctuations do not impact the overall performance of the battery. Post-cycling analyses confirmed that capacity losses in batteries assembled outside the glovebox were solely due to the SOC misbalance in the electrolytes when the reduced viologen was re-oxidized by oxygen, ruling out any irreversible degradation reactions of active species. Not significant variations in CVs were

10.1002/anie.202424650

observed after cycling, with similar redox potentials, peak separation, and no additional peaks compared to the fresh electrolytes (Figure 5d). Moreover, no extra peaks from degradation products or active species crossover were detected. To further verify that no electrolyte degradation occurred, UV-Vis measurements were performed after cycling at 50% SOC and compared to fresh samples at 0 and 100% SOC for both electrolytes (Figures 5e,f). As expected, both samples (catholyte and anolyte) show peaks corresponding to both charged and discharged species. In the case of the catholyte, peaks at 302, 322, and 423 nm are attributed to the charged species $[Fe(CN)_6]^{3-}$ and the broad peak at 330 nm is associated to the discharged species $[Fe(CN)_6]^{4-}$ (Figure 5e). Similarly, the spectrum of the anolyte after cycling reveals peaks at 368, 386, 397 and 602 nm, corresponding to the existence of $(SPr_2)V^{-}$ together with the signal of the discharged viologen (Figure 5f).[60] Moreover, post-cycling UV-VIS-analysis confirmed the high partitioning of active species in different oxidation states by the absence of peaks associated to ferro/ferricyanide in the anolyte and vice versa. Importantly, no additional peaks were detected in either the anolyte or catholyte samples suggesting that no degradation occurred. This finding is consistent with the results obtained from cyclic voltammetry which also shows no evidence of degradation (Figure 5d).

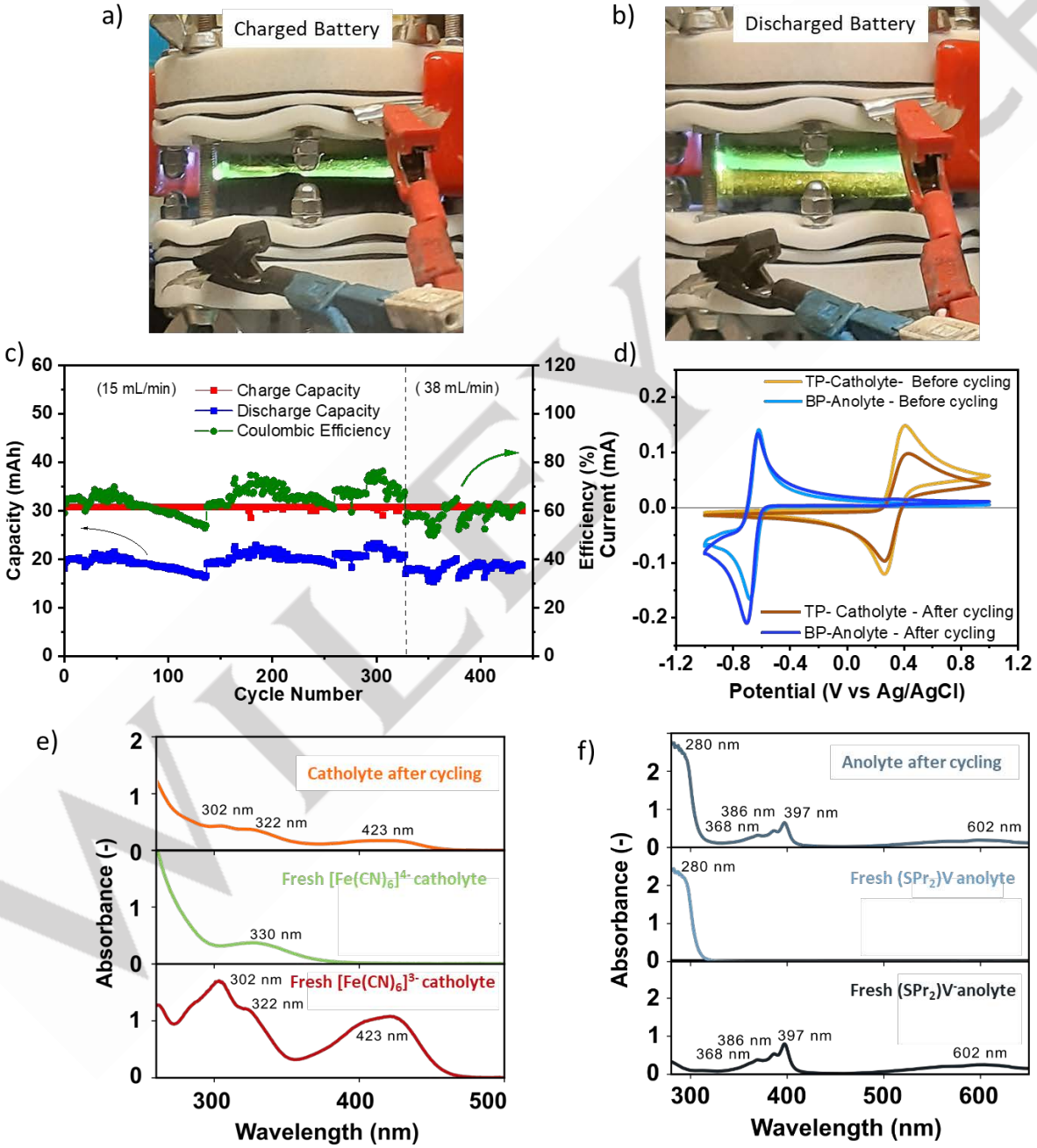

Figure 5. *Flow battery performance at pH 7, 0.1 M concentration of the active species. 21 mL each electrolyte. Theoretical capacity of 56.28 mAh, 2.68 Ah L^{-1}. a) and b) Photos of the cell at charged state and discharged state (a LED light was located behind the cell for better observation of the phases). c) Cyclability test 50%SOC at 3 mA cm^{-2}. c) Voltage profile during cycling. d) Crossover and degradation test. CV comparison between fresh and cycled electrolytes. UV-Vis spectra of e) a catholyte sample after cycling compared to 0 and 100% SOC samples of fresh catholyte, and f) an anolyte sample after cycling compared to 0 and 100% SOC samples of fresh anolyte.*

Conclusion

We propose a novel aqueous biphasic system (ABS) based on two salts, which offers excellent properties such as high ionic conductivity, low viscosity, and improved mass transport properties compared to previously used PEG-based ABS systems. The active species, namely ($K_4[Fe(CN)_6]$) and (SPr_2)V in their different charge states are effectively separated, which is a crucial factor for battery operation that has been largely overlooked previously. Partitioning properties were determined through computational methods and confirmed by CV, SECM, and UV-Vis spectroscopy. These proposed immiscible electrolytes also stand out for their chemical and electrochemical compatibility, not only ensuring effective separation by thermodynamics but also stable degradation from parasitic reactions. This stability enabled an in-depth study of the liquid-liquid interface, revealing new insights into interphase processes, such as the concentration gradient of each species and self-discharge reactions, without interference from side reactions. These results demonstrated that SECM is a capable tool to estimate the concentration gradient of the redox active species within the interface of two immiscible liquids system.

The corresponding membrane-free flow battery demonstrates significantly higher current and power density—more than 3.5 times greater than previous biphasic flow batteries—and improved cycling stability, with no capacity fade over more than one month of cycling (400 cycles). These findings highlight the improved electrolyte properties and overall performance stability of the new biphasic system.

This work advances critical aspects of membrane-free flow battery technology, including active species compatibility, interphase processes, and long-term battery performance. It does not only introduce a new aqueous electrolyte system with superior properties but also provides valuable insights that pave the way for further advancements in membrane-free battery technology.

Supporting Information

The authors have cited additional references within the Supporting Information.[51, 63]

Acknowledgements

The authors acknowledge the financial support by the Spanish Government (PID2021-124974OB-C21 and TED2021-129378B-C22), as well as the Light-cap and MeBattery projects which have received funding from the European Innovation Council (grant Agreements 101017821 and 101046742, respectively), and the MFreeB project which has received funding from the European Research Council (ERC) (grant agreement No. 726217). This work was partly funded by CICECO-Aveiro Institute of Materials, UIDB/50011/2020, UIDP/50011/2020, LA/P/0006/2020, financed by national funds through the FCT/MCTES (PIDDAC). The results reflect only the authors' view and the Agency is not responsible for any use that may be made of the information they contain.

Keywords: aqueous organic redox flow battery; membrane-free battery; redox species; scanning electrochemical microscopy; liquid-liquid interphase;

[1] International Energy Agency, *World Energy Outlook 2020*, **2020**.

[2] M. S. Ziegler, J. M. Mueller, G. D. Pereira, J. Song, M. Ferrara, Y. M. Chiang, J. E. Trancik, *Joule* **2019**, *3*, 2134–2153.

[3] E. Sánchez-Díez, E. Ventosa, M. Guarnieri, A. Trovò, C. Flox, R. Marcilla, F. Soavi, P. Mazur, E. Aranzabe, R. Ferret, *J. Power Sources* **2021**, *481*, 228804.

[4] L. F. Arenas, C. Ponce de León, F. C. Walsh, *Curr. Opin. Electrochem.* **2019**, *16*, 117–126.

[5] K. Lourenssen, J. Williams, F. Ahmadpour, R. Clemmer, S. Tasnim, *J. Energy Storage* **2019**, *25*, DOI 10.1016/j.est.2019.100844.

[6] P. Arevalo-Cid, P. Dias, A. Mendes, J. Azevedo, *Sustain. Energy Fuels* **2021**, *5*, 5366–5419.

[7] L. Tang, P. Leung, M. R. Mohamed, Q. Xu, S. Dai, X. Zhu, C. Flox, A. A. Shah, Q. Liao, *Electrochim. Acta* **2023**, *437*, 141460.

[8] C. T. de M. Gian Andrea Blengini, Cynthia EL Latunussa, Umberto Eynard, M. Dominic Wittmer, Konstantinos Georgitzikis, Claudiu Pavel, Samuel Carrara, Lucia Mancini, D. P. Unguru, Darina Blagoeva, Fabrice Mathieux, *Study on the EU ' s List of Critical Raw Materials*, **2020**.

[9] A. Trovò, G. Marini, W. Zamboni, S. D. Sessa, *Electron.* **2023**, *12*, 1844.

[10] A. Tang, J. Bao, M. Skyllas-Kazacos, *J. Power Sources* **2012**, *216*, 489–501.

[11] J. Ren, Y. Li, Z. Wang, J. Sun, Q. Yue, X. Fan, T. Zhao, *Int. J. Heat Mass Transf.* **2023**, *203*, 123818.

[12] W. Wang, V. Sprenkle, *Nat. Chem.* **2016**, *8*, 204–206.

[13] J. Luo, B. Hu, M. Hu, Y. Zhao, T. L. Liu, *ACS Energy Lett.* **2019**, *4*, 2220–2240.

[14] V. Singh, S. Kim, J. Kang, H. R. Byon, *Nano Res.* **2019**, *12*, 1988–2001.

[15] D. G. Kwabi, Y. Ji, M. J. Aziz, *Chem. Rev.* **2020**, *120*, 6467–6489.

[16] F. R. Brushett, M. J. Aziz, K. E. Rodby, *ACS Energy Lett.* **2020**, *5*, 879–884.

[17] M. A. Goulet, L. Tong, D. A. Pollack, D. P. Tabor, S. A. Odom, A. Aspuru-Guzik, E. E. Kwan, R. G. Gordon, M. J. Aziz, *J. Am. Chem. Soc.* **2020**, *141*, 8014–8019.

[18] S. R. Narayan, A. Nirmalchandar, A. Murali, B. Yang, L. Hoober-Burkhardt, S. Krishnamoorthy, G. K. S. Prakash, *Curr. Opin. Electrochem.* **2019**, *18*, 72–80.

[19] E. S. Beh, D. De Porcellinis, R. L. Gracia, K. T. Xia, R. G. Gordon, M. J. Aziz, *ACS Energy Lett.* **2017**, *2*, 639–644.

[20] C. Debruler, B. Hu, J. Moss, J. Luo, T. L. Liu, *ACS Energy Lett.* **2018**, *3*, 663–668.

[21] S. Hu, L. Wang, X. Yuan, Z. Xiang, M. Huang, P. Luo, Y. Liu, Z. Fu, Z. Liang, **2021**, *2021*, 1–8.

[22] Y. Liu, Y. Li, P. Zuo, Q. Chen, G. Tang, P. Sun, Z. Yang, T. Xu, *ChemSusChem* **2020**, *13*, 2245–2249.

[23] T. Janoschka, N. Martin, M. D. Hager, U. S. Schubert, *Angew. Chemie - Int. Ed.* **2016**, *55*, 14427–14430.

[24] J. Luo, B. Hu, C. Debruler, Y. Bi, Y. Zhao, B. Yuan, M. Hu, W. Wu, T. L. Liu, *Joule* **2019**, *3*, 149–163.

[25] P. Navalpotro, J. Palma, M. Anderson, R. Marcilla, *Angew. Chemie - Int. Ed.* **2017**, *56*, 12460–12465.

[26] P. Navalpotro, N. Sierra, C. Trujillo, I. Montes, J. Palma, R. Marcilla, *ACS Appl. Mater. Interfaces* **2018**, *10*, 41246–41256.

[27] K. Gong, F. Xu, M. G. Lehrich, X. Ma, S. Gu, Y. Yan, *J. Electrochem. Soc.* **2017**, *164*, A2590–A2593.

[28] A. F. Molina-Osorio, A. Gamero-Quijano, P. Peljo, M. D. Scanlon, *Curr. Opin. Electrochem.* **2020**, *21*, 100–108.

[29] M. O. Bamgbopa, Y. Shao-Horn, R. Hashaikeh, S. Almheiri, *Electrochim. Acta* **2018**, *267*, 41–50.

[30] X. Li, Z. Qin, Y. Deng, Z. Wu, W. Hu, *Adv. Sci.* **2022**, *2105468*, 2105468.

[31] S. Hou, L. Chen, X. Fan, X. Fan, X. Ji, B. Wang, C. Cui, J. Chen, C. Yang, W. Wang, C. Li, C. Wang, *Nat. Commun.* **2022**, *13*, 1–8.

[32] Z. Wang, J. Zhou, H. Ji, J. Liu, Y. Zhou, T. Qian, C. Yan, *Angew. Chemie Int. Ed.* **2024**, *63*, e202320258.

[33] P. Navalpotro, C. M. S. S. Neves, J. Palma, M. G. Freire, J. A. P. Coutinho, R. Marcilla, *Adv. Sci.* **2018**, *5*, 1–10.

[34] P. Navalpotro, C. Trujillo, I. Montes, C. M. S. S. Neves, J. Palma, M. G. Freire, J. A. P. Coutinho, R. Marcilla, *Energy Storage Mater.* **2020**, *26*, 400–407.

[35] P. Navalpotro, S. E. Ibañez, E. Pedraza, R. Marcilla, *Energy Storage Mater.* **2023**, *56*, 403–411.

[36] M. G. Freire, Ed. , *Ionic-Liquid- Based Aqueous Biphasic Systems Fundamentals and Applications*, Springer Berlin Heidelberg, **2016**.

[37] Y. Marcus, *J. Chem. Soc. Faraday Trans.* **1991**, *87*, 2995–2999.

[38] D. Dash, C. Mallika, U. Kamachi Mudali, *Chem. Prod. Process Model.* **2017**, *12*, 20160037.

[39] A. Klamt, *J. Phys. Chem.* **1995**, *99*, 2224–2235.

[40] A. Klamt, V. Jonas, T. Bürger, J. C. W. Lohrenz, *J. Phys. Chem. A* **1998**, *102*, 5074–5085.

[41] R. Santiago, F. H. Bordón Sosa, I. Díaz, M. González-Miquel, J. A. Pereira Coutinho, *Ind. Eng. Chem. Res.* **2023**, *62*, 17905–17913.

[42] J. P. Wojeicchowski, C. M. S. S. Neves, P. Navalpotro, R. Rubio-Presa, E. Ventosa, R. Marcilla, J. A. P. Coutinho, *J. Energy Storage* **2023**, *72*, 108584.

[43] W. Wu, A. P. Wang, J. Luo, T. L. Liu, *Angew. Chemie Int. Ed.* **2023**, *62*, e202216662.

[44] D. Reber, J. R. Thurston, M. Becker, M. P. Marshak, *Cell Reports Phys. Sci.* **2023**, *4*, 101215.

[45] E. M. Fell, D. De Porcellinis, Y. Jing, V. Gutierrez-Venegas, T. Y. George, R. G. Gordon, S. Granados-Focil, M. J. Aziz, *J. Electrochem. Soc.* **2023**, *170*, 070525.

[46] I. M. Kolthoff, E. A. Pearson, *Ind. Eng. Chem. Anal. Ed.* **1931**, *3*, 381–382.

[47] G. Wang, H. Zou, Z. Xu, A. Tang, F. Zhong, X. Zhu, C. Qin, M. Ding, W. You, C. Jia, *Mater. Today Energy* **2022**, *28*, 101061.

[48] T. Páez, A. Martínez-Cuezva, J. Palma, E. Ventosa, *J. Power Sources* **2020**, *471*, 228453.

[49] S. Jin, E. M. Fell, L. Vina-Lopez, Y. Jing, P. W. Michalak, R. G. Gordon, M. J. Aziz, *Adv. Energy Mater.* **2020**, *10*, 1–10.

[50] F. Li, P. R. Unwin, *J. Phys. Chem. C* **2015**, *119*, 4031–4043.

[51] J. Jedraszko, W. Nogala, W. Adamiak, E. Rozniecka, I. Lubarska-Radziejewska, H. H. Girault, M. Opallo, *J. Phys. Chem. C* **2013**, *117*, 20681–20688.

[52] E. Nieminen, N. Kazimova, L. Murtomäki, *Electroanalysis* **2020**, *32*, 949–957.

[53] H. Deng, P. Peljo, D. Momotenko, F. Cortés-Salazar, T. Jane Stockmann, K. Kontturi, M. Opallo, H. H. Girault, *J. Electroanal. Chem.* **2014**, *732*, 101–109.

[54] J. Zhang, A. L. Barker, P. R. Unwin, *J. Electroanal. Chem.* **2000**, *483*, 95–107.

[55] C. Wei, A. J. Bard, M. V Mirkin, *J. Phys. Chem.* **1995**, *99*, 16033–16042.

[56] D. Degoulange, R. Pandya, M. Deschamps, D. A. Skiba, B. M. Gallant, S. Gigan, H. B. de Aguiar, A. Grimaud, *Proc. Natl. Acad. Sci.* **2023**, *120*, e2220662120.

[57] I. Montes, R. Marcilla, J. Palma, E. Ventosa, M. Vera, M. Sánchez Sanz, S. E. Ibañez, *Redox Flow Battery with Immiscible Electrolyte and Flow through Electrode*, **n.d.**, WO2021209585A1.

[58] X. You, Q. Ye, P. Cheng, *J. Electrochem. Soc.* **2017**, *164*, E3386–E3394.

[59] J. D. Milshtein, K. M. Tenny, J. L. Barton, J. Drake, R. M. Darling, F. R. Brushett, *J. Electrochem. Soc.* **2017**, *164*, E3265–E3275.

[60] N. E. Holubowitch, A. Jabbar, *Microchem. J.* **2022**, *182*, 107920.

10.1002/anie.202424650

Entry for the Table of Contents

This study presents a new aqueous membrane-free flow battery based on a novel aqueous biphasic system with enhanced electrolyte properties. The system uses compatible species exhibiting high partitioning behavior, as demonstrated by computational and experimental analysis. These species prevent parasitic reactions, enabling unprecedented studies of the liquid-liquid interphase and providing valuable insights into advancing this battery technology.

Institute and/or researcher Twitter usernames: ((optional))